Development of a Riemann variables-based technique for on-line fuel injected mass evaluation in direct injection systems

Development of a Riemann variables-based technique for on-line fuel injected mass evaluation in direct injection systems

Zhang Tantan[(a)], Ferrari Alessandro[(b)], Vento Oscar[(b,*)]

(a) College of Mechanical and Vehicle Engineering, Hunan University, Changsha, China

(b) Energy Department, Politecnico di Torino, Turin, Italy

(*) Corresponding author. Email: oscar.vento@polito.it

Abstract

On-line evaluation of injected fuel mass based on physical principles offers the potential for accurate and rapid feedback on actual injection quantities. High-accuracy pressure transducers are commonly used as primary sensors to provide inputs for model-based virtual flowmeters. While increasing the number of transducers allows for a more comprehensive analysis of elementary waves within the system, balancing measurement accuracy and economic efficiency is essential for industrial applications.

In this study, a physics-based technique requiring only a single pressure sensor on the injector-feeding pipe is proposed, considering two elementary waves. The algorithm employs a predefined signal that exploits quasi-constant Riemann invariants propagating from the rail to the injector, enabling accurate estimation of the flow-rate and mass entering the injector. Correlation relationships are then used to convert the entering mass into the injected mass. This approach achieves an estimation accuracy within 2 mg for single injection events.

The proposed method is benchmarked against a previously developed flowmeter utilizing two pressure sensors, demonstrating that comparable accuracy can be obtained with a more economical single-sensor setup. The algorithm is applicable across a range of injection sizes and working conditions, offering a practical solution for real-time injected mass evaluation and control in high-pressure fuel systems.

Keywords

Direct Injection; Injected mass evaluation; closed-loop control; Characteristic curve; Elementary wave.

Nomenclature

A	pipe cross-sectional area
a	sound speed
C	chamber
C	constant
DT	dwell time
d	pipe diameter
E	elasticity modulus
ECU	electronic control unit
ET	energizing time
FMV	fuel metering valve
G	mass flow-rate
$\boldsymbol{H}$	vector of source terms
h	source term
I	energizing current
L	pipe length
M	fuel mass
PCV	pressure control valve
p	pressure
T	injection period
t	time
u	flow velocity
V	volume
$\boldsymbol{W}$	vector of characteristic variables
w	characteristic variable
x	space coordinate
$\boldsymbol{\Lambda}$	diagonal Jacobian matrix

ρ	density
τ	sheer stress

Subscripts

avg	averaged
cc	control chamber
$corr$	corrected
d	dynamic
f	finalize
$down$	transducer position positioned at the injector inlet
EOI	end of injection
inj	injected, injector
i	initial
in	inlet
nom	nominal
one	based on the innovative technique using one pressure transducer
out	fuel exiting an injector
$rail$	common-rail, rail side
SOC	start of current
s	static
two	based on the technique using two pressure transducers
up	transducer position close to the rail
w	wall
0	reference

1. Introduction

While electrification is at the forefront of research and development in the passenger car sector, the continued advancement of diesel-fueled internal combustion engines remains essential [1]. This is primarily due to their outstanding power density, which makes them particularly suitable for marine

propulsion and long-distance land transport applications [2]. Moreover, diesel engines are expected to contribute a significant share of CO_2 emissions well into the 2030s [3]. As a result, efforts to reduce emissions from diesel engines, including CO_2, are driven not only by increasingly stringent regulatory requirements [4], but also by the overarching goal of achieving carbon neutrality in the coming decades [5].

In recent years, considerable research has been devoted to reducing carbon emissions from diesel engines. Key strategies include advancements in injection technologies [6], optimization of combustion chamber geometry [7], and the adoption of fuel blends [8]. Concerning injection systems, common-rail systems [9] have been in existence for over two decades, and they have evolved into indispensable components of contemporary diesel engines. Simultaneously, the effective implementation of specific control strategies in a common-rail system relies on accurate and stable control of the fuel dosage for each injection. Despite this, industrial applications of common-rail systems typically rely on open-loop control strategies, regulating injected fuel quantity using calibrated parameters such as nominal rail pressure (p_{nom}) and energizing time (ET) of the electrical current signal [10]. These parameters are mapped in the engine control unit (ECU) based on extensive pre-calibration experiments under various operating conditions. As a result, the actual injected mass during real-time engine operation remains unmeasured. Preliminary studies have shown that accurate closed-loop control of injected fuel mass can significantly reduce engine-out CO_2 emissions [11]. Therefore, the development of an affordable and robust technique for online evaluation of injected fuel quantity is of great importance.

Existing online measurement methods for fuel injections are typically classified into two main groups: those based on engine combustion models and those utilizing mechanical-hydraulic models of the injection system. The latter can be further divided into two types: one that extracts a few scalar quantities from continuous signals within a single engine cycle, and another that employs the entire acquired signal time history as model input.

Techniques based on combustion models acquire performance-related data for each engine cycle. The fuel injected quantity is determined through simplified and empirical models. For instance, Finesso et al. [12] derived the injected mass by measuring the in-cylinder pressure. This method involves the inversion of a predictive combustion model [13]. Initially, the heat release rate is ascertained based on

110 the measured pressure signal within the combustion chamber, and the injected fuel mass can be
111 estimated using predefined ignition delay and the combustion rate of the heat release model. However,
112 these methods require intricate modeling and careful calibration, and the simplified models are typically
113 accurate only within limited operating conditions.

114 Mechanical-hydraulic model-based approaches focusing on scalar features use empirical
115 corrections to address errors in traditional ECU calibration maps. Ferrari et al. [14] implemented a time-
116 frequency-based virtual needle-lift sensor [15] to detect nozzle opening and closing events, correlating
117 injected mass with nozzle opening duration. Payri et al. [16] proposed a mathematical model using
118 inputs such as rail pressure (p_{rail}), ET and back pressure. After injector characterization, where a set
119 of coefficients is determined for the mathematical expressions and correlations, the model can compute
120 both injected flow-rate and quantity. Similarly, Ma et al. [17] evaluated the injected quantity by
121 monitoring p_{rail} reduction, introducing a parameter K (the pressure decline rate) as an indicator. Such
122 approaches are mainly used in industry for ECU feedback. Advanced injector-integrated sensors, such
123 as Bosch's NCS (Needle Closing Sensor) [18] and DENSO's i-ART injector [19] utilize injector internal
124 pressure time histories to estimate injected mass through needle-lift-based models [20]. Delphi's Switch
125 technology provides a practical means of detecting needle positions in non-ballistic injectors [21].
126 While these approaches balance model complexity and practicality, they primarily serve as
127 compensatory strategies and are sensitive to factors like thermal regimes, which can affect accuracy.

128 Recently, machine learning techniques have been introduced to predict injected quantity or flow-
129 rate. Williams et al. [22] developed two machine learning algorithms to estimate the injection rate of a
130 common-rail injection system using only a single input signal of p_{rail}, though such reliance may lead
131 to errors in identifying needle events when pressure waves from other injectors propagate in the rail.
132 In [23], the injected flow-rate of a piezoelectric injector was estimated using an artificial neural network
133 algorithm, which received four different input parameters: injection pressure, measuring chamber
134 pressure and temperature, and command signal duration. Deep learning models, such as those in [24],
135 have been developed for multi-injection scenarios using rail pressure and current signal features as
136 inputs. However, these approaches often function as "black-box" models and require large training
137 datasets, which can limit interpretability [25].

Mechanical-hydraulic methods that process entire signal histories directly estimate representative flow-rates or nozzle outflow, and integration over time provides the total injected quantity per cycle. Yang et al. [26] extracted pilot-main injection rates from pressure signals near the injector inlet via a lumped electrical model, decoupling water hammer effects and applying needle-lift modeling, though this remains limited to non-ballistic injectors. The Bosch method enables estimation of pipe internal flow rate for small injections using a single sensor [27]. However, this is invalid when pressure waves reflected from the rail reach the transducer after nozzle opening.

In such cases, Euler equations must be combined with additional pressure time data [28], with subsequent integration yielding pipe-passed mass, which is correlated to the injected mass. Nonetheless, the precise relationship between internal pipe flow and nozzle outflow remains unclear, and most physics-based methods require at least two pressure sources for large injections, making them less generalizable. Thus, a method that provides comparable accuracy while requiring only a single pressure transducer per injector would be more practical for industrial application.

In this study, a previously developed flowmeter is implemented on the rail-to-injector pipe of a common-rail injection system to evaluate the space-averaged internal fuel flow-rate. We conduct a comprehensive analysis of both static and dynamic leakage under a wide range of single injection operating conditions, and further elucidate the complex relationship among internal pipe flow, leakage, and injected mass. Building on a validated one-dimensional numerical model, we propose an innovative method for determining the internal flow rate using only a single pressure sensor. This method leverages quasi-constant Riemann invariants propagating from the rail to the injector, and utilizes a predetermined signal, partially captured by the flowmeter. Finally, two algorithms are employed to evaluate the injected fuel mass, with a comparative analysis of their results, and the potential application of this approach as a control strategy is discussed.

2. Experimental facility

The experimental campaign was conducted at the Politecnico di Torino ICE Laboratory using a Moehwald-Bosch hydraulic test bench with a nominal power of 35 kW, a maximum speed of 6100 rpm, and a maximum torque of 100 Nm. Temperature and pressure levels within the high-pressure hydraulic

circuit were monitored using an array of thermocouples and piezoresistive pressure transducers mounted along the investigated high-pressure hydraulic circuit. As reported in Figure 1, an HDA flowmeter is employed to measure the injected flow-rate traces and the corresponding masses [29], and the injector leakages were quantified with a Coriolis flowmeter. The electric command signal to the injector was accurately measured employing a current clamp. Moreover, pressure signals near the rail (p_{up}) and near the injector (p_{down}) along the injector-feeding pipe were recorded with a National Instruments PXI system at a sampling frequency of 30 kHz.

Shell V-Oil 1404 (ISO 4113) was selected as the calibration fluid, accurately replicating the properties of renewable diesel under relevant pressure and temperature conditions (up to 120 °C) [30]. For the test campaign, a Bosch CR system from the latest generation was employed as the injection system. A high-pressure pump, with a 430 mm^3 displacement and a single double-acting piston, supplies the rail and features a 1:1 transmission ratio. This rail is connected to four solenoid-actuated CRI 2.20 injectors via 320 mm long, 2.7 mm internal diameter high-pressure pipes.

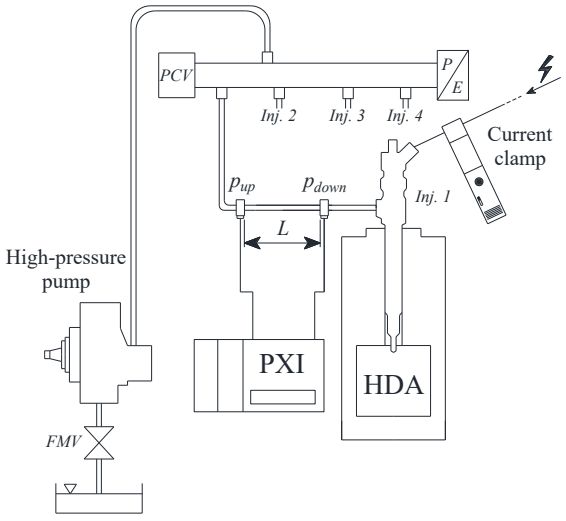

Figure 1. Injection system layout.

The ECU utilizes a PID controller to regulate p_{rail}. The PID controller input is determined by the discrepancy between the measured pressure inside the rail and the target rail pressure value. The pressure control valve (cf. PCV in Figure 1), located at one end of the rail, modulates excess pumped fuel based on the duty cycle received from the PID pressure controller. Simultaneously, the duty cycle

is directed to the fuel metering valve (cf. FMV in Figure 1), positioned at the pump inlet, to adjust the flow-rate being drawn in, thereby preventing fuel from being throttled by the PCV.

The pilot stage includes a pressure-balanced pilot valve, and the injector integrates a Minirail. Figure 2 illustrates the layout of the tested injector.

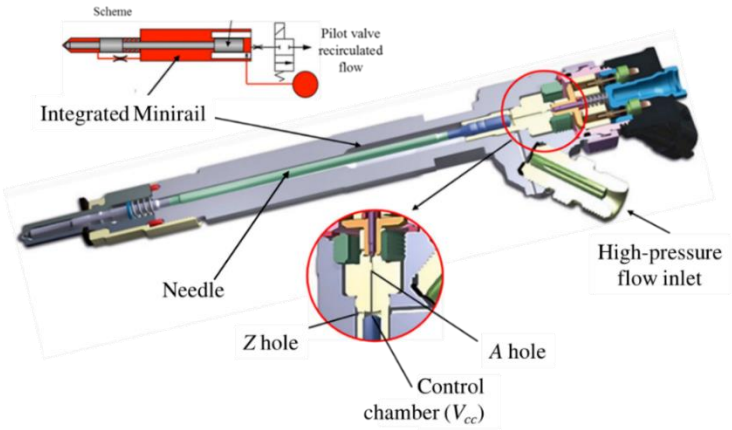

Figure 2. Injector CRI 2.20.

In terms of the injector operating principle, a significant portion of the fuel is directed to the integrated Minirail, while the remainder enters the control chamber (volume V_{cc}) through the Z hole. The ECU activates the pilot valve solenoid by suppling the electrical current I, initiating the injection process. Consequently, fuel is discharged from the control chamber through the A hole, facilitating the upward movement of the needle, which opens the nozzle. Following the cessation of the ECU current signal, signifying the initiation of the needle closing phase, the control chamber pressure begins to rise once more. The injection cycle concludes when the needle makes contact with the nozzle as it reaches the downstroke end.

For varying ET values, single injections have been taken into consideration, with nominal pressure p_{nom} ranging from 800 and 1800 bar. The chosen pump speed for the entire testing campaign was set at 2000 rpm, corresponding to an engine speed of 2000 rpm.

3. Flowmeter based on incompressible flow assumption

Focusing on the rail-to-injector pipe (i.e., the section equipped with the p_{up} and p_{down} pressure transducers, as shown in Figure 1), and assuming an isothermal process, the energy equation reduces to

206 the equation of state. Accordingly, the pipe can be represented as a one-dimensional slender tube,
207 governed by the generalized Euler partial differential equations for mass and momentum conservation
208 [31]:

209 $$\frac{\partial}{\partial t}\begin{bmatrix}\rho\\ \rho u\end{bmatrix}+\frac{\partial}{\partial x}\begin{bmatrix}\rho u\\ \rho u^2+p\end{bmatrix}=\begin{bmatrix}0\\ -4\tau_w/d\end{bmatrix} \quad (1)$$

210 where x and t denote the spatial and temporal coordinate. u, p, ρ represent the 1D flow velocity, the
211 pressure and the density, respectively. τ_w signifies the wall shear stress, which is determined through
212 the Darcy-Weisbach equation. Assuming incompressible flow, the continuity equation simplifies to
213 $\frac{\partial u}{\partial x}=0$, and consequently, the momentum balance equation can be expressed as:

214 $$\frac{\partial u}{\partial t}+\frac{1}{\rho}\frac{\partial p}{\partial x}=-\frac{4\tau_w}{\rho d} \quad (2)$$

215 where d is the pipe internal diameter. Integrating over the length L (the distance between p_{up} and
216 p_{down} cf. Figure 1) and multiplying by $\rho A/L$, where A stands for the pipe cross-section area, Eq. (2)
217 becomes:

218 $$\frac{d\overline{G}}{dt}=\frac{A}{L}\Delta p-\pi d\overline{\tau_w} \quad (3)$$

219 where G represents the mass flow-rate and $\Delta p=p_{up}-p_{down}$, and the overlined quantities are space-
220 averaged. Integrating Eq. (3) with respect to time yields the space-averaged flow-rate time history:

221 $$\overline{G}(t)=\overline{G}_0+\int_0^t\frac{A}{L}\Delta p dt-\pi d\int_0^t\overline{\tau_w}dt \quad (4)$$

222 where $\overline{G}_0$ is the initial value of $\overline{G}(t)$. Integrating Eq. (4) over an entire cycle, the friction term can
223 be expressed in terms of the time-average of the pressure difference Δp as [32]:

224 $$\overline{G}(t)=\overline{G}_0+\frac{A}{L}\int_0^t[\Delta p-\langle\Delta p\rangle]dt \quad (5)$$

225 where angular brackets represent the time-averaged quantities. As inferred from Eq. (5), the
226 instantaneous mass flow-rate can be determined by measuring the Δp along the considered pipe with
227 an offset $\overline{G}_0$. Since the rail-to-injector pipe is investigated, the measured $\overline{G}(t)$ in Eq. (5) corresponds
228 to the mass flow-rate $G_{inj,in}$ at the injector inlet. The presented flowmeter has been already tested
229 satisfactorily on gear pumps [33], [34] and on a GDI injection system [35].

4. Correlation between fuel injected mass and injector inlet/leakage mass

By applying Eq. (5) to evaluate $G_{inj,in}$, it is crucial to first establish its initial value $\overline{G}_0$. This can be assumed to be the flow-rate entering the injector, which is the portion throttled by the closed pilot stage (known as static leakage, denoted as $G_{leak,s}$). The measurement of static leakages was performed using the Coriolis flowmeter, with the ET set to zero while the hydraulic system was pressurized. The results for $G_{leak,s}$ at different p_{nom} are presented Table 1.

Table 1. Static leakages for different nominal pressure levels.

p_{nom} [bar]	400	600	800	1000	1200	1400	1600	1800
$G_{leak,s}$ [g/min]	1.95	2.10	2.3	3.3	4.5	6.6	9.8	13.3

Figure 3 illustrates the space-averaged flow-rate along the rail-to-injector pipe entering the injector (line with symbols), the injected flow-rate (continuous red line), and the current signal (dashed line) for a single injection with $p_{nom} = 1200$ bar and $ET = 620$ µs. The injection event generates pressure waves that propagate along the rail-to-injector pipe and can locally induce negative flow-rates. These reverse flows, typically observed after the end of injection, result from fluid dynamic interactions within the high-pressure pipe and are induced by water hammer effects caused by the rapid closure of the injector's needle.

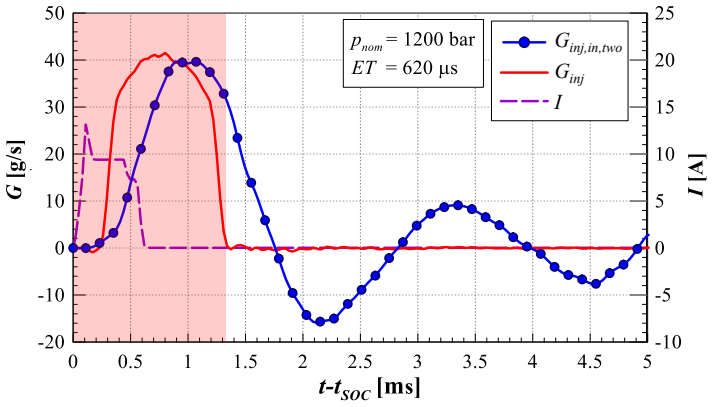

Figure 3. Flow-rate entering the injector, injected flow-rate and current signal.

Regarding the mass exiting the injector, two distinct contributions are considered: the mass injected through the nozzle holes and the mass flow throttled by the pilot stage. The Coriolis flowmeter, installed

249 at the pilot stage outlet, measures the latter during injection cycles but cannot provide instantaneous
250 flow-rate data. Therefore, it only yields a time-averaged flow-rate, denoted as $G_{leak,Coriolis}$.

251 Considering the instantaneous flow-rate going through the pilot stage, it can be approximated that
252 over an entire injection cycle, $G_{leak,Coriolis}$ aligns with the static value measured when $ET = 0$ µs
253 (as indicated in Table 1). However, it increases when the ECU provides a current signal to the injector
254 solenoid. Figure 4 illustrates the values of $G_{leak,Coriolis}$ for different ET values at varying p_{nom}.

255 If one considers an injection period T, the instantaneous flow-rate through the pilot stage (denoted
256 as $G_{leak,real}$) and the time-averaged flow-rate $G_{leak,coriolis}$ measured by the Coriolis flowmeter are
257 linked by the following relation

258 $$\int_0^T G_{leak,real}dt = \int_0^T G_{leak,Coriolis}dt \quad (6)$$

259 Therefore, the dynamic leakage mass, denoted as $M_{leak,d}$ and corresponding to the flow throttled by
260 the pilot stage when it is open, can be calculated for each operating condition as:

261 $$M_{leak,d} \equiv \int_0^T (G_{leak,real} - G_{leak,s})dt = \int_0^T (G_{leak,Coriolis} - G_{leak,s})dt \quad (7)$$

262 With regard to the mass entering the injector, this quantity can be obtained by integrating $G_{inj,in}$ over
263 the relevant time interval, and is expressed as:

264 $$M_{inj,in} \equiv \int_{t_i}^{t_f} G_{inj,in}dt \quad (8)$$

265 where t_i corresponds to the time instant t_{SOC}, at which the energizing current starts to rise (i.e., $t -$
266 $t_{SOC} = 0$ ms in Figure 3), while t_f is defined as follows. Assuming the injector can be modeled as a
267 0D chamber with a given pressure time history p_{inj}, and with different flow-rates entering and leaving
268 the domain, the continuity equation can be written as:

269 $$\frac{V_{inj}}{a^2}\int_{t_i}^{t_f} dp_{inj} = \int_{t_i}^{t_f}(G_{inj,in} - G_{inj} - G_{leak})dt = M_{inj,in} - M_{inj} - M_{leak} = M_{inj,in} - M_{out} \quad (9)$$

270 where a represents the fuel sound speed, defined as $a = \sqrt{dp/d\rho}$, V_{inj} denotes the volume of the
271 0D chamber modeling the injector, and M_{out} represents the mass of fuel exiting the injector. Eq. (9)
272 reveals that a balance between the inlet and outlet masses $M_{inj,in} = M_{inj} + M_{leak} = M_{out}$ is achieved
273 when the integration interval is chosen such that $p_{inj}(t_i) = p_{inj}(t_f)$, implying $\int_{t_i}^{t_f} dp_{inj} = 0$.

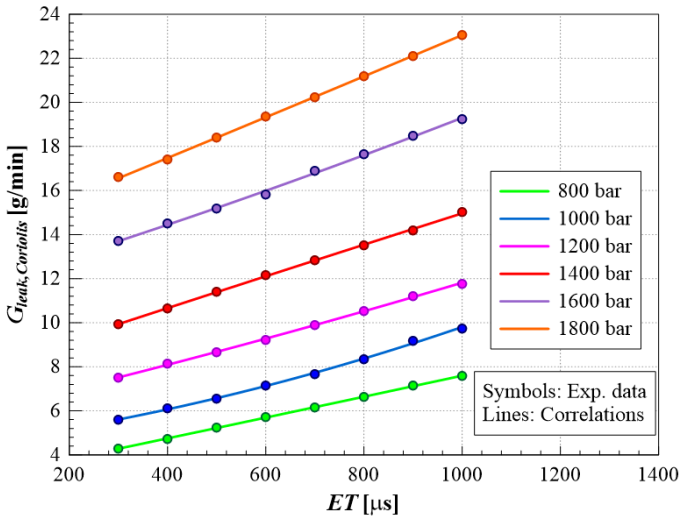

Figure 4. Injector pilot stage throttled flow-rates for different ET and p_{nom} values.

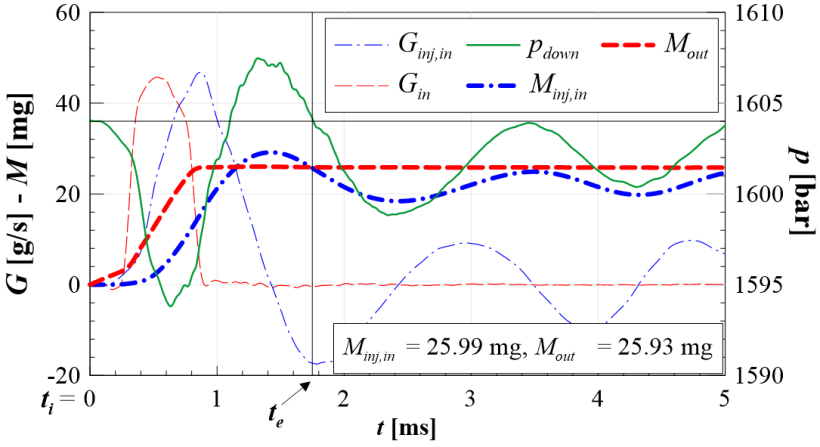

Figure 5. Definition of the end of integration to calculate the mass entering the injector.

Although real injectors have more complex hydraulic circuits than a 0D chamber, the pressure signal p_{down}, measured near the injector inlet, can serve as a representative pressure for the internal hydraulic circuit. For an injection with $p_{nom} = 1600$ bar and $ET = 400$ μs, Figure 5 shows the injector inlet mass flow-rate $G_{inj,in,two}$ (thin blue dash-dot curve), the injected mass flow-rate G_{inj} (thin red dashed curve), and the pressure time history p_{down} (solid green curve). The figure also displays the cumulative values of $G_{inj,in,two}$, denoted as $M_{inj,in,two}$ (thick blue dash-dot curve), and M_{out}, which is calculated as the sum of the injected flow-rate and the flow-rate throttled by the pilot stage (thick dashed red curve). It is noteworthy that the data related to variables with subscript two were evaluated using the aforementioned technique, which applies the incompressible flow assumption and utilizes two pressure time histories.

By selecting $p_{down}(t_f) = p_{down}(t_{SOC})$, the instant t_f marks the moment when the injector inlet

pressure returns to its initial value at t_{SOC}. Although the wave dynamics in the rail-to-injector pipe are still active, this condition provides a state that most closely resembles the pressure state at t_{SOC}. In Figure 5, this moment corresponds to $t_f \approx 1.75$ ms, as indicated by the intersecting black solid line. At this point, the curves of $M_{inj,in,two}$ and M_{out} intersect, satisfying the mass balance described in Eq. (9).

As the values of $M_{inj,in,two}(t_f)$ are calculated over a wide range of working points (82 in total), a correlation between $M_{inj,in,two}(t_f)$ vs $M_{out}(t_f)$, as shown in Figure 6, can be determined. This correlation closely follows the bisector line, confirming the validity of the flowmeter concept according to Eq. (9).

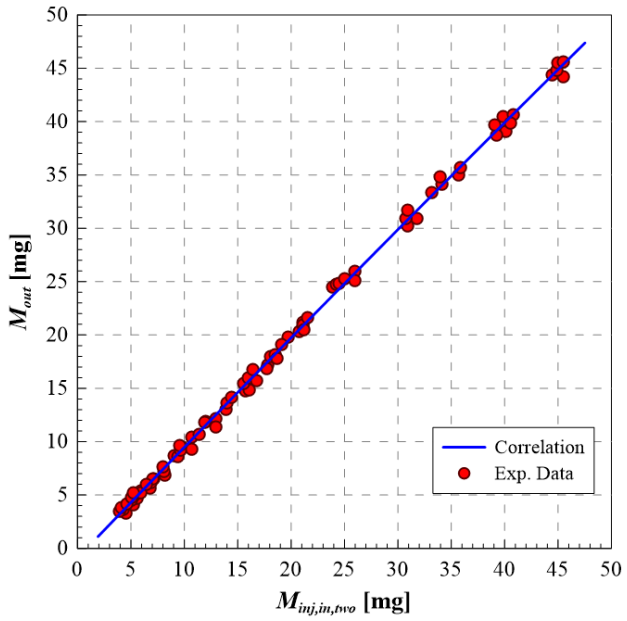

Figure 6. Correlation between the mass entering the injection and the outlet one.

The maximum and average errors stand at 1.12 mg and 0.39 mg, respectively. This close agreement between $M_{inj,in,two}$ and M_{out} further demonstrates the viability of the flowmeter concept. The proposed approach provides a reliable benchmark for high-pressure transient mass flow-rate assessment, paving the way for the development of an innovative on-line flowmeter that relies on a single pressure transducer.

5. Elementary wave analyses of rail-to-injector pipe internal flow

The barotropic numerical model of the injection system, previously developed and validated, is shown in Figure 7. This model comprehensively incorporates the vital attributes of the hydraulic circuit, mechanical configuration, and electromagnetic elements. It takes inputs of p_{rail} and I trace acting on the solenoid.

The hydraulic circuit is composed of interconnected 0D chambers linked by 1D pipes, with some pipes featuring gauged orifices at their extremities. The initial conditions are specified as uniform pressure and zero velocity for the fluid states. Within the model, the pipes are describe using Eq. (1). The influencing forces are a result of hydraulic, mechanical, and electromagnetic processes, with the moving components following ordinary differential forms of Newton's laws of motion.

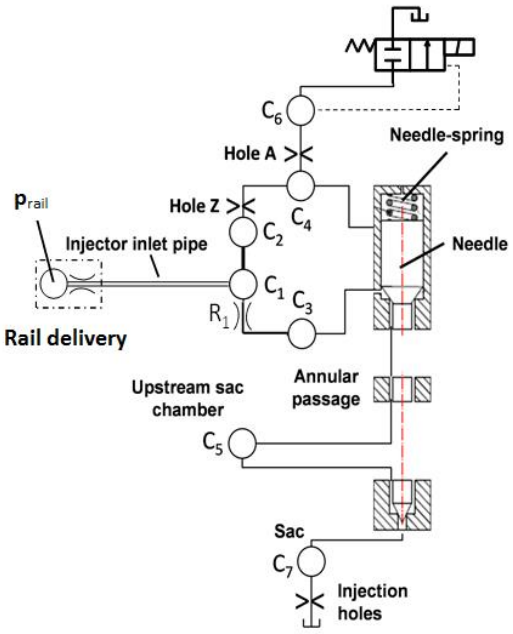

Figure 7. Schematic of the 1D hydraulic-mechanical- numerical model.

Given that the sound speed remains below 0.02 Mach number across all operating conditions, Eq. (1) reduces to a set of quasi-linear hyperbolic partial differential equations [36]. Consequently, the system can be decoupled into a series of advection equations with source terms, expressed as:

$$\frac{\partial \boldsymbol{W}}{\partial t} + \boldsymbol{\Lambda}\frac{\partial \boldsymbol{W}}{\partial x} = \boldsymbol{H} \tag{10}$$

where $\boldsymbol{\Lambda}$ is the diagonalized Jacobian matrix of the system, defined as:

$$\boldsymbol{\Lambda} = \begin{bmatrix} u-a & 0 \\ 0 & u+a \end{bmatrix} \tag{11}$$

$\boldsymbol{W}$ represents the characteristic variables, and its differential form is written as:

$$\delta\boldsymbol{W} = \begin{bmatrix} \delta w_1 \\ \delta w_2 \end{bmatrix} = \begin{bmatrix} \delta u - (a/\rho)\delta\rho \\ \delta u + (a/\rho)\delta\rho \end{bmatrix} \tag{12}$$

and $\boldsymbol{H}$ is the source term:

$$\boldsymbol{H} = \begin{bmatrix} h_1 \\ h_2 \end{bmatrix} = \begin{bmatrix} 4\tau_w/\rho d \\ -4\tau_w/\rho d \end{bmatrix} \tag{13}$$

As the fuel properties, in accordance with the ISO 4113 standard, are described using a fitting method, it has been previously demonstrated in [37] that the characteristic variables can be expressed as follows:

$$\boldsymbol{W} = \begin{bmatrix} W_1 \\ W_2 \end{bmatrix} = \begin{bmatrix} u - 2\cdot\rho_0^{-\frac{1}{2}}\cdot E_0^{\frac{1}{2\chi}}\cdot\frac{(E_0+\chi p)^{\frac{1}{2}-\frac{1}{2\chi}}}{\chi-1} + C_1 \\ u + 2\cdot\rho_0^{-\frac{1}{2}}\cdot E_0^{\frac{1}{2\chi}}\cdot\frac{(E_0+\chi p)^{\frac{1}{2}-\frac{1}{2\chi}}}{\chi-1} + C_2 \end{bmatrix} \tag{14}$$

where ρ_0 and E_0 indicate the density and elasticity modulus at a reference pressure, and χ is an intermediate variable dependent on temperature. Since the model assumes an isothermal process, ρ_0, E_0 and χ remain constants in this model.

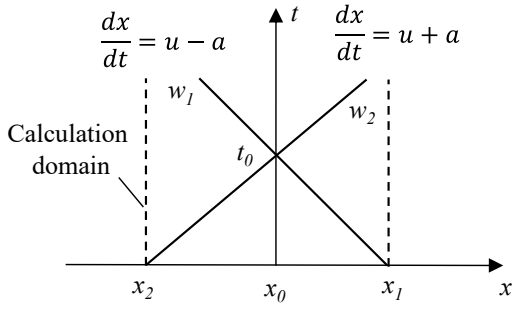

Figure 8. Characteristic curves for the tube model.

Figure 8 provides a schematic of the propagation of characteristic variables in the space-time domain. The two solid lines represent the characteristic curves of the system governed by Eqs. (10)-(13). Their slopes $(dx/dt = x \mp a)$ correspond to the eigenvalues of Eq. (10), as defined in Eq. (11), and indicate the wave propagation speeds. Since the Mach number remains below 0.02 in the high-pressure circuit for all operating conditions, the eigenvalues are always one negative and one positive. The variables w_1 and w_2 evolve temporally at rates specified by Eq. (11), propagating along their

respective characteristics. Additionally, the absence of shockwaves under these conditions ensures that numerical errors from the finite difference solution of the decoupled system are negligible. By transitioning from an Eulerian to a Lagrangian framework, Eq. (10) can be reformulated as a set of ordinary differential equations, given by:

$$\frac{d\boldsymbol{W}}{dt} = \boldsymbol{H} \tag{15}$$

where $\boldsymbol{W}$ and $\boldsymbol{H}$ represent the corresponding variables in Eq. (12)-(14), while each elementary wave front of the characteristic variable is analyzed individually. For instance, a wavefront of w_1 (or w_2) traveling at a speed of $u - a$ (or $u + a$) is tracked over time, and its state is described by Eq. (15).

A single hydraulic injection represents a highly transient hydrodynamic process. Elementary waves are generated within the high-pressure circuit due to pressure fluctuations from the high-pressure pump or internal hydraulic-mechanical effects in the injector [38]. Figure 9 schematically illustrates the propagation of these waves along the injector-feeding pipe: w_1 propagates from the injector toward the rail, while w_2 travels in the opposite direction, from the rail to the injector.

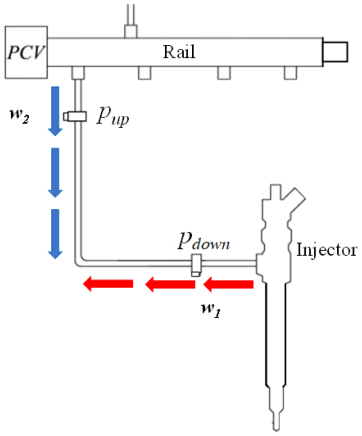

Figure 9. Schematic of elementary waves.

Figure 10 presents simulated time histories of the two waves at both ends of the pipe when $p_{nom} = 800$ bar and $ET = 600$ μs. In this figure, $w_{1,inj,in}$ and $w_{2,inj,in}$ represent the time distributions of w_1 and w_2 at the injector inlet, while $w_{1,rail}$ and $w_{2,rail}$ denote the same variables at the rail-pipe interface. As established in Figure 9, the waves $w_{1,inj,in}$ and $w_{2,rail}$, propagating at the injector inlet side and at the rail side, respectively, are of particular interest, since they reflect within the considered domain (the rail-to-injector pipe). Meanwhile, the constants C_1 and C_2 in Eq. (14) can be arbitrarily

defined, as only the variation of w_1 and w_2 along the pipe are relevant. Therefore, C_1 and C_2 are set such that $w_{1,inj,in}$ and $w_{2,rail}$ are zero at t_{SOC}. The initial evolution of $w_{1,rail}$ and $w_{2,inj,in}$ depends on the pre-t_{SOC} values of $w_{1,inj,in}$ and $w_{2,rail}$, during which p and u changes are negligible. Thus, identical values of C_1 and C_2 can be assigned throughout the injection phase. Specifically, $C_1 = 2 \cdot \rho_0^{-\frac{1}{2}} \cdot E_0^{\frac{1}{2\chi}} \cdot (E_0 + \chi p(t_{SOC}))^{\frac{1}{2}-\frac{1}{2\chi}}/(\chi - 1)$ and $C_2 = -2 \cdot \rho_0^{-\frac{1}{2}} \cdot E_0^{\frac{1}{2\chi}} \cdot (E_0 + \chi p(t_{SOC}))^{\frac{1}{2}-\frac{1}{2\chi}}/(\chi - 1)$ are used consistently.

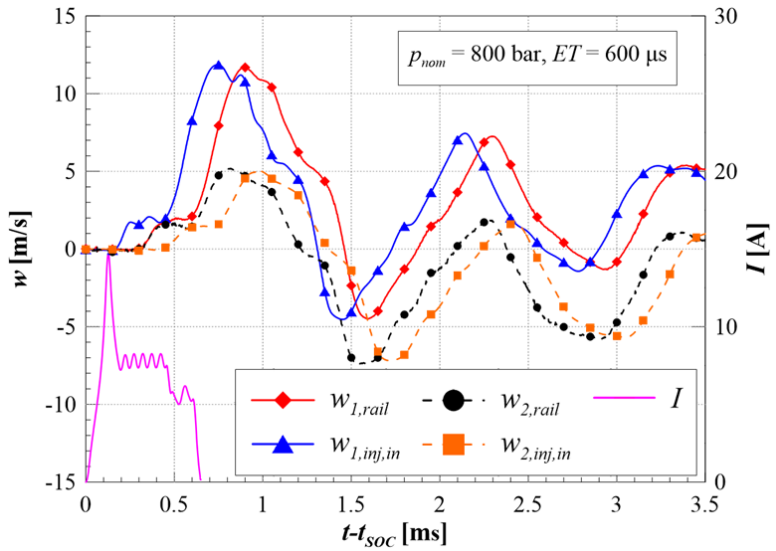

Figure 10. Elementary waves traveling from the rail-to-end pipe extremities.

It can be observed that when a wave propagates from one side to the other, a time lag appears between the wavefronts at these two locations due to the finite wave speeds, as given in Eq. (11). Additionally, both $w_{1,rail}$ and $w_{2,rail}$ deviate from zero simultaneously, triggered by the arrival of the none-zero wavefront $w_{1,inj,in}$ at the rail side. The variable w_2 contains all information about the wave reflected at the connector, and traveling toward the injector. Notably, as $w_{1,inj,in}$ propagates to $w_{1,rail}$, the peak amplitude decreases, a phenomenon also observed as $w_{2,rail}$ transforms into $w_{2,inj,in}$. This reduction in peak values indicates energy dissipation due to friction, as described by the source term in Eq. (13) and the right-hand side of Eq. (15).

6. Injected mass evaluation based on elementary wave analyses

As reported in [37], the time profiles of the reflected wave w_2 at the rail-pipe connector are nearly

identical within a specific range of operating conditions from t_{SOC} to a certain point after hydraulic injection. This interval, highlighted in red in Figure 3, indicates that $w_{2,rail}$ can be treated as a constant time history across a various rail pressures during this period, from t_{SOC} to t_{EOI} (end of the injection). Since the injector-feeding pipe hydrodynamics are governed by Eq. (10), a system of two hyperbolic partial differential equations, knowledge of the time evolution of w_2 at a fixed spatial location enables the system to be simplified to a single advection equation with w_1 as the only unknown. This allows the internal mass flow rate in the pipe to be determined using just a single pressure signal and a pre-determined $w_{2,rail}$ profile. The injected mass can then be calculated analytically.

According to Eq. (14), w_1 contains the variables of p and u, both dependent on time and space, along with other state variables. At the injector side of the pipe, p is measured directly by a pressure transducer (p_{down},) at $x_{inj,in}$, while $u_{inj,in}$ cannot be measured directly.

Figure 11 provides an ad-hoc scheme for evaluating $u_{inj,in}$. The spatial domain, illustrated in Figure 11, extends from the rail–pipe joint (x_{rail}) to the location of the pressure transducer $x_{inj,in}$. $w_{2,rail,avg}$ denotes the average time evolution of $w_{2,rail}$ at the rail-pipe joint. Since the time profile of $w_{2,rail}$ under different operating conditions are similar between t_{SOC} and t_{EOI}, an average time history $w_{2,rail,avg}$ can be constructed and effectively represents $w_{2,rail}$ for a broad range of working conditions.

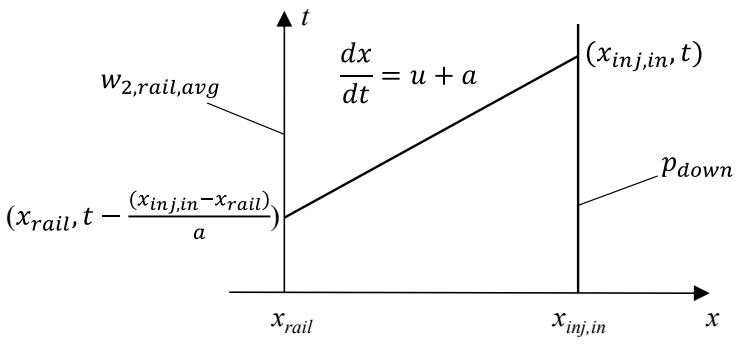

Figure 11. Flow velocity evaluation based on elementary wave analyses.

At any given instant t, the value of $w_{2,rail,avg}(t)$ propagates downstream at a speed of $u + a$, with its evolution described by Eq. (15). Given that the Mach number remains consistently below 0.02 across all operating conditions, substituting $u + a$ with a introduces a negligible error in the wave

transmission speed estimation.

During the initial period, $t - t_{SOC} \leq (x_{inj,in} - x_{rail})/a$, $w_{2,inj,in}$, which corresponds to w_2 at the spatial coordinate of $x_{inj,in}$, remains constant, unaffected by the elementary wave transmitted from the rail side. Thus, variation in $u_{inj,in}$ are directly related to changes in $p_{inj,in}$, in accordance with the Bosch method [27]. Immediately after $t - t_{SOC} = (x_{inj,in} - x_{rail})/a$, the property $w_{2,inj,in}(t)$ can be determined from $w_{2,rail,avg}$, and $u_{inj,in}$ for both two phases can be calculated using the following equation:

$$u_{inj,in}(t) = \begin{cases} P(t_{SOC}) - P(t) & \text{if } t - t_{SOC} \leq (x_{inj,in} - x_{rail})/a \\ w_{2,rail,avg}(t - \frac{x_{inj,in} - x_{rail}}{a}) + P(t_{SOC}) - P(t) & \text{if } t - t_{SOC} > (x_{inj,in} - x_{rail})/a \end{cases} \quad (16)$$

where $P(t)$ is a function of p_{down} expressed as

$$P(t) = 2 \cdot \rho_0^{-\frac{1}{2}} \cdot E_0^{\frac{1}{2\chi}} \cdot \frac{(E_0 + \chi p_{down}(t))^{\frac{1}{2} - \frac{1}{2\chi}}}{\chi - 1} \quad (17)$$

It is crucial to highlight that $P(t_{SOC})$ plays a key role in setting the initial value of $w_{2,rail,avg}$ when an injection initiates, ensuring that $w_{2,rail,avg}(t_{SOC}) = 0$ through the appropriate selection of C_2. Eqs. (16) and (17) link the measurable signal $p_{inj,in}$ to the target variable $u_{inj,in}$. As w_2 propagates from the rail to the injector inlet, it is affected by the wall shear stress, as described in Eq. (15). Consequently, the values of $w_{2,rail,avg}$ are iteratively updated as the wavefront travels toward $x_{inj,in}$, with the initial value of $u_{inj,in}$ from Eq. (16). This iterative adjustment is performed at each sample point using:

$$w_{2,inj,in}^{n+1} = w_{2,rail,avg}^{n} - \frac{f}{2} \frac{\left|u_{inj,in}^{n}\right| u_{inj,in}^{n}}{d} \cdot \frac{x_{inj,in} - x_{rail}}{a} \quad (18)$$

where n represents the number of iterations, and f stands for the friction factor. Furthermore, $u_{inj,in}^{n}$, which is involved in the next iteration calculation, is determined based on Eq. (14) using $w_{2,inj,in}^{n}$, p_{down}, and the determined C_2.

The in-pipe mass flow rate is then determined as:

$$G_{inj,in} = \rho A u_{inj,in} \quad (19)$$

The injected mass can be estimated using integration and correlation methods similar to those employed in the aforementioned flowmeter shown in Section 4, under the assumption of incompressible flow.

7. Results of the hydraulic tests and discussion

In the application of the evaluation method based on elementary wave analyses, $w_{2,rail,avg}$ serves as a predefined signal, formed by combining the pressure and velocity data at the rail-pipe connector across various working conditions. While the pressure signal can be directly obtained through a sensor (cf. p_{up} in Figure 1) during the algorithm setup phase, the velocity time history cannot be directly captured by any transducer.

Figure 12 presents simulated flow velocity and pressure time histories at both ends of the pipe that feeds the injector for a typical operating condition ($p_{nom} = 800$ bar and $ET = 600$ µs). u_{rail} and $u_{inj,in}$ exhibit similar trends, particularly during the initial rise and fall phases, though they intersect occasionally. This similarity suggests that the velocity component (u_{rail}) of the predefined signal $w_{2,rail}$ can be approximated using the space-averaged flow rate between the pressure time histories p_{up} and p_{down} (see Figure 1), as calculated by the incompressible flow assumption-based flowmeter described in Eq. (5). In Figure 12, u_{avg} is calculated from simulated p_{rail} and $p_{inj,in}$.

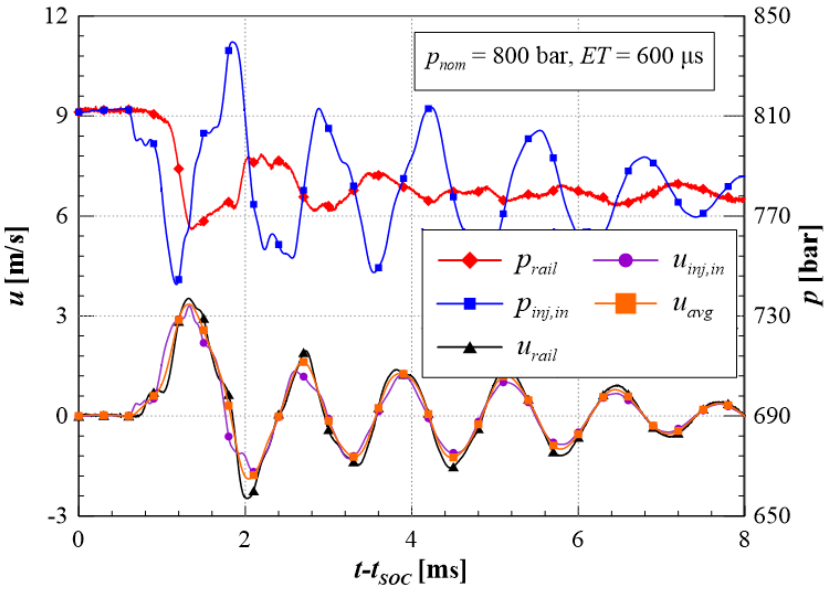

Figure 12. Time histories of the flow velocities at the extremities of pipe feeding the injector.

Notably, u_{rail} lags slightly behind $u_{inj,in}$ for $t - t_{SOC} < 2$ ms. Since the space-averaged velocity u_{avg} mainly represents the pipe center fluid property, and $w_{2,rail,avg}$ necessitates u_{rail} at the rail-pipe connector, a time-shift of u_{avg} in time is necessary. Therefore, a delay of 90 µs is

introduced to u_{avg}, corresponding to a propagation distance of approximately 15 cm, based on the speed of sound in ISO 4113 oil. The final $w_{2,rail}$ signal is then derived using Eq. (14), with this delayed u_{avg} and the p_{up} signal, which approximates p_{rail} at the rail-pipe joint (located about 5 cm from the p_{up} sensor).

Figure 13 presents all $w_{2,rail}$ time histories (thin colored curves) involved in the averaging calculation for a wide range of operating conditions, along with the derived $w_{2,rail,avg}$ (thick black curve) used for injected mass evaluation. To minimize the error between $w_{2,rail,avg}$ and each $w_{2,rail}$ over the valid temporal length, the working conditions are segregated into two categories, respectively for p_{nom} ranging from 800 to 1200 bar and from 1400 to 1800 bar. This separation is necessary because the value of a in Eq. (16) is predefined for each pressure range, and the resulting error in a within a single category can be as large as 100 m/s. Grouping the working conditions in this way reduces the error in a thereby improving the accuracy of injected mass evaluation. It is worth noting that only the segments between t_{SOC} and t_{EOI} of $w_{2,rail}$ for the considered operating conditions are included in the averaging, and only one curve tail of $w_{2,rail}$ for a large injection after its t_{EOI}, positioned at the center of the curve family, is not truncated in order to smoothen out the final averaged signal. Within each category, all curves of $w_{2,rail}$ are averaged across different operating conditions over the valid time range. Additionally, a Butterworth filter is applied to smooth the averaged signal $w_{2,rail,avg}$ while retaining its primary physical information. Consequently, it is evident that $w_{2,rail,avg}$ is situated at the center of $w_{2,rail}$ and closely correlates with these $w_{2,rail}$ in each category.

Figure 14 presents the estimated injector inlet fuel mass flow-rates $G_{inj,in,one}$ (blue squares) for two typical cases following Eqs. (16)–(19) based on $w_{2,rail,avg}$ plotted in Figure 13. The estimated mass flow-rate $G_{inj,in,two}$ (red curves), evaluated based on the method described in Eq. (5) and previously validated in the literature [11], is used as a reference to assess the feasibility of the new approach.

Figure 14(a), representing a small injection, $G_{inj,in,one}$ closely follows $G_{inj,in,two}$ until $t - t_{SOC} \approx 0.8$ ms, beyond which the two curves begin to diverge. This divergence occurs because $w_{2,rail}$

also deviates from $w_{2,rail,avg}$ under these conditions. However, during the interval from t_{SOC} to the instant when p_{down} first return to its value at ($p_{down}(t_f) = p_{down}(t_{SOC})$), the agreement remains strong, validating the use of the single-sensor estimate up to this point.

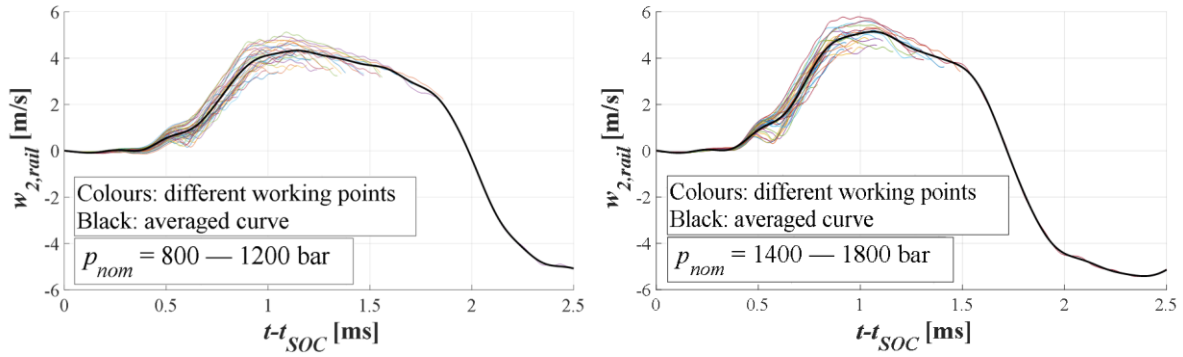

(a) **(b)**

Figure 13. $w_{2,rail}$ time histories when p_{nom} between 800 bar and 1800 bar: (a) $p_{nom} = 800 - 1200$ bar; (b) $p_{nom} = 1400 - 1800$ bar.

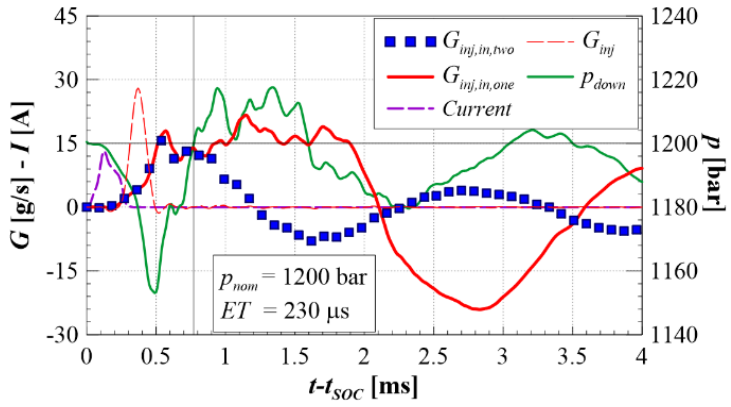

(a)

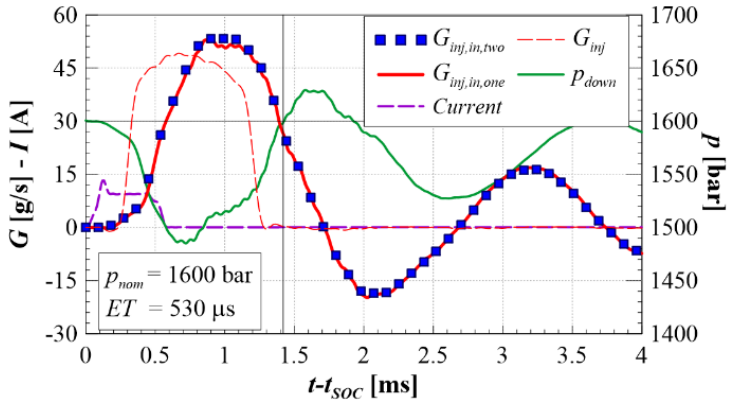

(b)

Figure 14. Comparison between the methods applying one or two pressure sensors: (a) $p_{nom} = 1200$ bar and $ET = 230$ µs; (b) $p_{nom} = 1600$ bar and $ET = 530$ µs.

Figure 14(b) presents a similar graph for a large injection. As the $w_{2,rail,avg}$ presents the average of $w_{2,rail}$ across a range of working conditions, and large injections exhibit longer valid $w_{2,rail}$ phase during the evaluation of $w_{2,rail,avg}$. As a result, $G_{inj,in,one}$ and $G_{inj,in,two}$ are nearly overlapped. This signifies that the estimated injector inlet flow-rate remains valid until a slightly later instant after t_{EOI}.

Given the lack of an obvious integration endpoint with the single-sensor approach, t_f is defined as the time when p_{down} first returns to its initial value ($p_{down}(t_f) = p_{down}(t_{SOC})$), which is approximately $t - t_{SOC} \approx 0.7$ ms in Figure 14(a) and $t - t_{SOC} \approx 1.4$ ms in Figure 14(b) The total mass passing through the pipe is then computed by integrating $G_{inj,in,one}$ over its valid time interval:

$$M_{inj,in,one} = \int_{t_{SOC}}^{t_f} G_{inj,in,one} dt \tag{20}$$

Figure 15 plots the HDA-measured hydraulic injected fuel mass M_{inj} versus $M_{inj,in,one}$. Although the operating conditions are categorized into two families based on p_{nom} (cf. Figure 13), Figure 15 unmistakably reveals a significant correlation between M_{inj} and $M_{inj,in,one}$. The correlations (blue curves) in Figure 15 follows linear trend with a maximum observed error of 1.7 mg.

The predictive performance is further illustrated in Figure 16, where the estimated injected mass $M_{inj,one}$ calculated using the fitted function $M_{inj,one} = f(M_{inj,in,one})$, is plotted against M_{inj}. The data closely follow the bisector line, with a maximum deviation of 2 mg and an average error of 0.6 mg, indicating that the method is reliable for control applications due to its minimal margin of error.

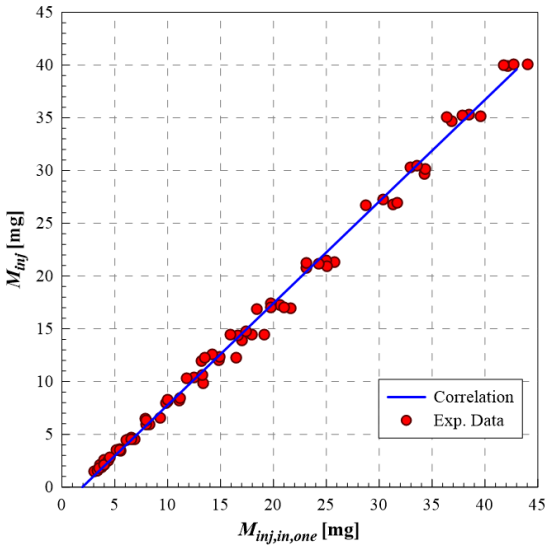

Figure 15. Correlation between M_{inj} and $M_{inj,in,one}$ for evaluation method employing one sensor.

Turning to double injections, Figure 17 shows $w_{2,rail}$ curves corresponding to different dwell time (DT), with identical ETs for both injections. It is evident that $w_{2,rail}$ fails to converge throughout the entire hydraulic injection phase for multiple injections, as all curves diverge immediately at the onset of the second injection.

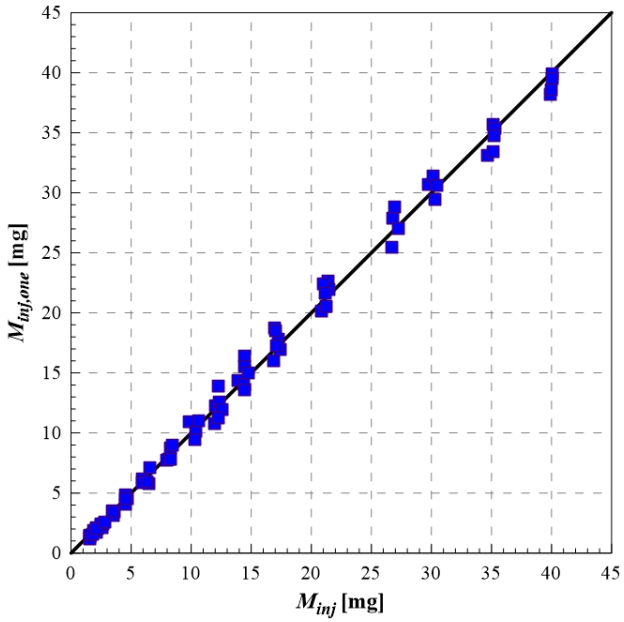

Figure 16. Prediction performance of the M_{inj} vs $M_{inj,in,one}$ correlation.

Consequently, while the proposed technique is not applicable for measuring injected mass in

multiple injection scenarios, it provides accurate and robust estimates for the first injection, independent of its size or the presence of reflected waves during the event.

It is worth highlighting that the methodology presented here is broadly applicable to all liquid fuels, including OMEx and methanol, because it relies solely on the assumption of incompressible flow.

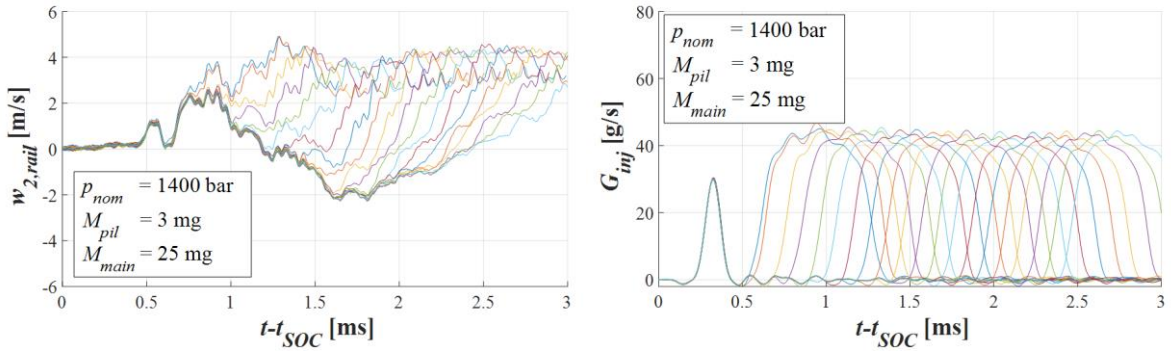

(a) **(b)**

Figure 17. Time distributions of $w_{2,rail}$ and G_{inj} for pilot-main injections with different DT values: (a) $w_{2,rail}$; (b) G_{inj}.

As already presented in the literature [11, 35], the mass entering the injector can be used to set up a closed-loop strategy for the injected mass. A possible scheme for this closed-loop control is presented in Figure 18. During an injection event, the acquired p_{down} signal is used together with the stored $w_{2,rail,avg}$ pattern to work-out the entering flow-rate. This flow-rate is integrated to calculate the entering mass and, by means of the correlation presented in Figure 18, the injected mass can be estimated ($M_{inj,one}$). Such an estimation is compared with the target value of fuel quantity (M_{target}) and the difference $\Delta M_{inj} = M_{target} - M_{inj,one}$ is provided as an input value of a PID controller: the output of this PID controller is an energizing time correction (ΔET), that is employed to provide a new ET value (ET_{corr}) to the injector, that will compensate the injected mass inaccuracy.

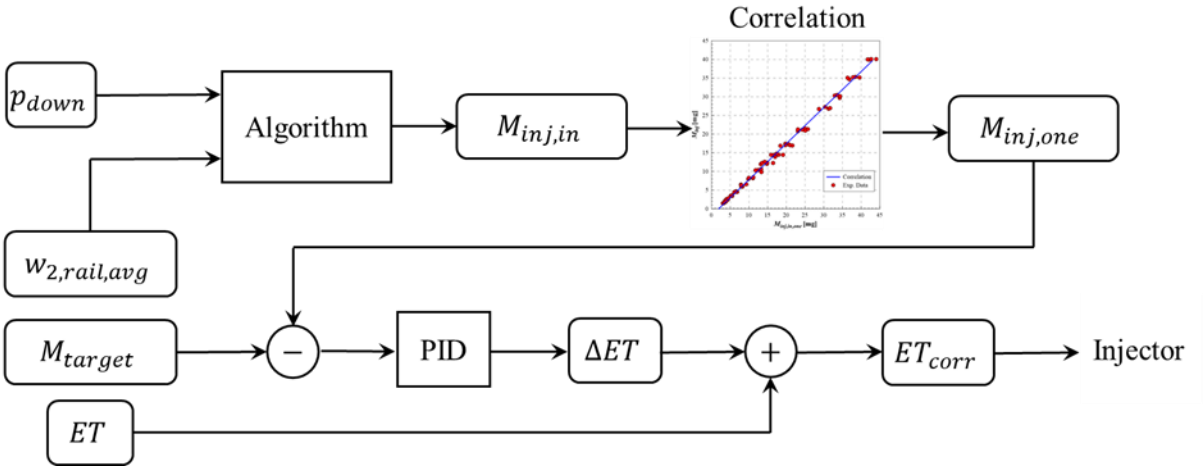

Figure 18. Example of a possible closed-loop control strategy for the ET correction.

8. Conclusions

- A strong bisector correlation was observed between the fuel mass passing through the injector-feeding pipe and the total outflow, comprising both injected and leaked mass.
- The injected mass was estimated using a hyperbolic PDE system characterized by two elementary waves; one wave is obtained from the measured pressure, while the other is predefined based on the convergence behavior of first injections.
- The proposed method accurately estimates the fuel flow-rate from t_{SOC} to the point when p_{down} returns to its initial pressure level at t_{SOC}, using only a single pressure transducer.
- The estimated injected mass achieves an error within 2 mg, with an average deviation of 0.6 mg.
- The injected mass estimation can be employed to set-up a closed loop control for the injected mass to compensate inaccuracy of the fuel quantity.

Acknowledgements

This work was financially supported by National Natural Science Foundation of China (52406046) and Natural Science Foundation of Hunan Province (2024JJ6147).

[1] E. Shafiei, R. Dauphin, and M. Yugo, "Optimal electrification level of passenger cars in Europe in a battery-constrained future," *Transp Res D Transp Environ*, vol. 102, p. 103132, Jan. 2022, doi: 10.1016/J.TRD.2021.103132.

[2] L. Liu, Y. Peng, W. Zhang, and X. Ma, "Concept of rapid and controllable combustion for high

power-density diesel engines," *Energy Convers Manag*, vol. 276, p. 116529, Jan. 2023, doi: 10.1016/J.ENCONMAN.2022.116529.

[3] G. Magnolia, M. Gambini, S. Mazzoni, and M. Vellini, "Renewable energy, carbon capture & sequestration and hydrogen solutions as enabling technologies for reduced CO2 energy transition at a national level: an application to the 2030 Italian national energy scenarios," *Cleaner Energy Systems*, vol. 4, p. 100049, Apr. 2023, doi: 10.1016/J.CLES.2022.100049.

[4] P. Ni, X. Wang, and H. Li, "A review on regulations, current status, effects and reduction strategies of emissions for marine diesel engines," *Fuel*, vol. 279, p. 118477, Nov. 2020, doi: 10.1016/J.FUEL.2020.118477.

[5] B. Wang, C. Yang, H. Wang, D. Hu, and Y. Wang, "Effect of Diesel-Ignited Ammonia/Hydrogen mixture fuel combustion on engine combustion and emission performance," *Fuel*, vol. 331, p. 125865, Jan. 2023, doi: 10.1016/J.FUEL.2022.125865.

[6] M. Güler and M. Özkan, "Energy balance analysis of a DI diesel engine with multiple pilot injections strategy and optimization of brake thermal efficiency," *Appl Therm Eng*, vol. 204, p. 117972, Mar. 2022, doi: 10.1016/J.APPLTHERMALENG.2021.117972.

[7] Y. Kang, X. Li, H. Shen, Y. Chen, D. Liu, and J. Chang, "Effects of combustion chamber diameter on the performance and fuel–air mixing of a double swirl combustion system in a diesel engine," *Fuel*, vol. 324, p. 124392, Sep. 2022, doi: 10.1016/J.FUEL.2022.124392.

[8] R. Elumalai and K. Ravi, "Strategy to reduce carbon emissions by adopting ammonia–Algal biodiesel in RCCI engine and optimize the fuel concoction using RSM methodology," *Int J Hydrogen Energy*, vol. 47, no. 94, pp. 39701–39718, Dec. 2022, doi: 10.1016/J.IJHYDENE.2022.09.169.

[9] T. Kato, T. Koyama, K. Sasaki, K. Mori, and K. Mori, "Common Rail Fuel Injection System for Improvement of Engine Performance on Heavy Duty Diesel Engine," Feb. 1998. doi: 10.4271/980806.

[10] T. Wintrich *et al.*, "Motorsysteme," 2015, pp. 165–211. doi: 10.1007/978-3-658-08861-3_4.

[11] A. Ferrari, C. Novara, E. Paolucci, O. Vento, M. Violante, and T. Zhang, "Design and rapid prototyping of a closed-loop control strategy of the injected mass for the reduction of CO2,

combustion noise and pollutant emissions in diesel engines," *Appl Energy*, vol. 232, 2018, doi: 10.1016/j.apenergy.2018.09.028.

[12] R. Finesso and E. Spessa, "A control-oriented approach to estimate the injected fuel mass on the basis of the measured in-cylinder pressure in multiple injection diesel engines," *Energy Convers Manag*, vol. 105, pp. 54–70, Nov. 2015, doi: 10.1016/J.ENCONMAN.2015.07.053.

[13] A. E. Catania, R. Finesso, and E. Spessa, "Predictive zero-dimensional combustion model for DI diesel engine feed-forward control," *Energy Convers Manag*, vol. 52, no. 10, pp. 3159–3175, Sep. 2011, doi: 10.1016/J.ENCONMAN.2011.05.003.

[14] A. Ferrari, Z. Jin, O. Vento, and T. Zhang, "An injected quantity estimation technique based on time–frequency analysis," *Control Eng Pract*, vol. 116, 2021, doi: 10.1016/j.conengprac.2021.104910.

[15] A. Ferrari and F. Paolicelli, "A virtual injection sensor by means of time frequency analysis," *Mech Syst Signal Process*, vol. 116, pp. 832–842, Feb. 2019, doi: 10.1016/J.YMSSP.2018.07.009.

[16] R. Payri, J. Gimeno, R. Novella, and G. Bracho, "On the rate of injection modeling applied to direct injection compression ignition engines," *International Journal of Engine Research*, vol. 17, no. 10, pp. 1015–1030, Dec. 2016, doi: 10.1177/1468087416636281.

[17] X. Ma, Y. Lei, T. Qiu, J. Wang, and G. Yue, "Investigation of fuel injection rate identification algorithm based on rail pressure fluctuation characteristics induced by injection," *Proceedings of the Institution of Mechanical Engineers, Part D: Journal of Automobile Engineering*, vol. 236, no. 6, pp. 1101–1114, May 2022, doi: 10.1177/09544070211039312.

[18] J. Hammer, M. Raff, and D. Naber, "Advanced diesel fuel injection equipment – A never ending BOSCH story," 2014, pp. 31–45. doi: 10.1007/978-3-658-05130-3_4.

[19] T. Miyaura, A. Morikawa, Y. Ito, K. Ishizuka, and T. Tsuiki, "Development of Diesel Engine using New Fuel Injection System - Direct Monitoring of Fuel Injection Pressure using Injector with Built-in Sensor, and its Applications," Apr. 2013. doi: 10.4271/2013-01-1739.

[20] K. Serizawa, D. Ueda, N. Mikami, Y. Tomida, and J. Weber, "Realizing Robust Combustion with High Response Diesel Injector with Controlled Diffusive Spray Nozzle and Closed Loop

614 Injection Control," Mar. 2017. doi: 10.4271/2017-01-0845.
615 [21] P. Voigt *et al.*, "Delphi Injector Closed Loop Control Strategy Using the 'Switch' Technology
616 for Diesel Passenger Cars – Injector Hardware," 2017, pp. 41–66. doi: 10.1007/978-3-658-
617 15327-4_3.
618 [22] Z. Williams *et al.*, "Generation of Rate-of-Injection (ROI) profile for Computational Fluid
619 Dynamics (CFD) model of Internal Combustion Engine (ICE) using machine learning," *Energy
620 and AI*, vol. 8, p. 100148, May 2022, doi: 10.1016/j.egyai.2022.100148.
621 [23] E. Choi, J. Park, J. Hwang, H. Oh, J. Manin, and H. S. Sim, "Injection rate measurements and
622 Machine-Learning based predictions of ECN Spray A-3 piezoelectric injector," *Appl Therm Eng*,
623 vol. 254, p. 123827, Oct. 2024, doi: 10.1016/j.applthermaleng.2024.123827.
624 [24] X. Lu, J. Zhao, V. Markov, and T. Wu, "Study on precise fuel injection under multiple injections
625 of high pressure common rail system based on deep learning," *Energy*, vol. 307, p. 132784, Oct.
626 2024, doi: 10.1016/J.ENERGY.2024.132784.
627 [25] A. Ferrari, S. Gurrì, and O. Vento, "Injected Fuel Mass and Flow Rate Control in Internal
628 Combustion Engines: A Systematic Literature Review," *Energies (Basel)*, vol. 17, no. 24, p.
629 6455, Dec. 2024, doi: 10.3390/en17246455.
630 [26] X. Yang, Q. Dong, J. Song, and T. Zhou, "Investigation of a method for online measurement of
631 injection rate for a high-pressure common rail diesel engine injector under multiple-injection
632 strategies," *Meas Sci Technol*, vol. 33, no. 2, p. 025301, Feb. 2022, doi: 10.1088/1361-
633 6501/ac3548.
634 [27] A. Ferrari and F. Paolicelli, "An indirect method for the real-time evaluation of the fuel mass
635 injected in small injections in Common Rail diesel engines," *Fuel*, vol. 191, pp. 322–329, Mar.
636 2017, doi: 10.1016/j.fuel.2016.11.053.
637 [28] A. Ferrari, C. Novara, E. Paolucci, O. Vento, M. Violante, and T. Zhang, "A new closed-loop
638 control of the injected mass for a full exploitation of digital and continuous injection-rate
639 shaping," *Energy Convers Manag*, vol. 177, 2018, doi: 10.1016/j.enconman.2018.08.037.
640 [29] A. Ferrari and T. Zhang, "Benchmark between Bosch and Zeuch method–based flowmeters for
641 the measurement of the fuel injection rate," *International Journal of Engine Research*, vol. 22,

no. 1, pp. 316–327, Jan. 2021, doi: 10.1177/1468087419827732.

[30] A. Ferrari and O. Vento, “Thermal effects on Common Rail injection system hydraulic performance,” *International Journal of Engine Research*, p. 146808742311624, Mar. 2023, doi: 10.1177/14680874231162412.

[31] Z. Jin *et al.*, “Numerical-experimental optimization of the common-feeding injection system concept for application to light-duty commercial vehicles,” *Journal of Energy Resources Technology, Transactions of the ASME*, vol. 143, no. 12, 2021, doi: 10.1115/1.4050133.

[32] A. Ferrari and P. Pizzo, “Optimization of an Algorithm for the Measurement of Unsteady Flow-Rates in High-Pressure Pipelines and Application of a Newly Designed Flowmeter to Volumetric Pump Analysis,” *J Eng Gas Turbine Power*, vol. 138, no. 3, Mar. 2016, doi: 10.1115/1.4031541.

[33] A. Corvaglia, A. Ferrari, M. Rundo, and O. Vento, “Three-dimensional model of an external gear pump with an experimental evaluation of the flow ripple,” *Proc Inst Mech Eng C J Mech Eng Sci*, vol. 235, no. 6, 2021, doi: 10.1177/0954406220937043.

[34] A. Ferrari, P. Fresia, M. Rundo, O. Vento, and P. Pizzo, “Experimental Measurement and Numerical Validation of the Flow Ripple in Internal Gear Pumps,” *Energies (Basel)*, vol. 15, no. 24, 2022, doi: 10.3390/en15249607.

[35] A. Ferrari, P. Pizzo, and O. Vento, “Investigation of a GDI injector with an innovative flowmeter for high-pressure transient flows,” *International Journal of Engine Research*, Jul. 2023, doi: 10.1177/14680874231187552.

[36] E. F. Toro, *Riemann Solvers and Numerical Methods for Fluid Dynamics*. Berlin, Heidelberg: Springer Berlin Heidelberg, 2009. doi: 10.1007/b79761.

[37] T. Zhang, “An estimation method of the fuel mass injected in large injections in Common-Rail diesel engines based on system identification using artificial neural network,” *Fuel*, vol. 310, p. 122404, Feb. 2022, doi: 10.1016/j.fuel.2021.122404.

[38] M. Baratta, A. E. Catania, and A. Ferrari, “Hydraulic Circuit Design Rules to Remove the Dependence of the Injected Fuel Amount on Dwell Time in Multijet CR Systems,” *J Fluids Eng*, vol. 130, no. 12, Dec. 2008, doi: 10.1115/1.2969443.